Progress In Electromagnetics Research B, Vol. 30, 371–387, 2011

USING CORRELATION MAPS IN A WIDE-BAND MICROWAVE GPR

A. Di Donato[1, *], M. Farina[2], A. Morini[1], G. Venanzoni[1], D. Mencarelli[1], M. Candeloro[1], and M. Farina[1]

[1]Dipartimento di Ingegneria Biomedica, Elettronica e Telecomunicazioni, Universit Politecnica delle Marche, Ancona 60131, Italy

[2]MEM Research, Pescara 65010, Italy

Abstract—This paper describes the use of the correlation maps in the Ground Penetrating Radar (GPR) for the detection of near surface objects. This method is based on the definition of bi-dimensional maps that describe the level and the nature of coherence between the received electromagnetic signals. The technique proposed provides the detection of objects, reducing the impact of the clutter and improving the image contrast by an appropriate combination of the information collected in the variance and time coherence of the received signals. The method has been tested in GPR developed by ourselves and described in detail. The implemented GPR system features a high dynamic vector network analyzer (VNA) and a mechanically scanned Vivaldi antenna; the scanning is bi-dimensional, so that A, B and C scans are available.

1. INTRODUCTION

Ground Penetrating Radars (GPR) have been used for a number of applications, spanning from the detection of defects in structures and buildings, detection of pipes and cables in the soil, geological research, land-mine detection [1–4] and estimation of relative permittivity of shallow soil [5]. Using microwaves is one of the considered options, apparently faced with an intrinsic contradiction, i.e., the need for high frequencies in order to achieve the needed spatial resolution and, at the same time, the requirement of low frequencies in order to guarantee a sufficient penetration in the soil. Actually the first constraint (high frequency for high resolution) is a consequence of the so called "Abbe's

Received 3 May 2011, Accepted 22 May 2011, Scheduled 24 May 2011

* Corresponding author: Andrea Di Donato (a.didonato@univpm.it).

barrier", linking the spatial resolution limit to the radar wavelength. However since 70s it has been shown that using evanescent microwave field (the "near"-field) allows to breach such a barrier [6]: as matter of fact waves in the order of centimeters are currently used to achieve sub-micrometric surface microscopy [7]. Hence it is possible to exploit the lower part of the spectrum to penetrate lossy soils. In the wide-band GPR the amount of information collected is usually very high and it is hence important to have a tool that allows to recognize quickly the buried object and define its main physical features, by avoiding at the same time that significant information be lost during the data manipulation. Different approaches have been used in wide-band microwave GPR to get data and images of buried objects in unknown medium [1]. According to the measurement arrangement and data acquisition scheme, there are two different techniques usually employed: the monostatic or bistatic data acquisition. In this work the images have been acquired by means of a monostatic system, in which the same probe is used as a source and receiver of the electromagnetic waves. In the past, very large efforts have been spent in post-processing analysis of GPR data, that have lead to the development of different techniques, such as: data migration, focusing, filtering, SAR based algorithms, inverse scattering calculation, e.g., [8–12]). Moreover, approaches in background subtraction have been realized; an exhaustive description is reported in [1]. The GPR signal analysis presented in this work is based on the mapping of some relevant statistical parameters related to the level of coherence of the received signals, such as the co-variance, the coherence time and the correlation coefficient, in order to detect buried objects. The use of the correlation function in the wide-band GPR signals detection is well known. In the least square or matched filters the sampled time series are filtered in such a way that the output is an impulse function representing the de-convolution of the wanted signal. As a consequence, a matched filter is mathematically identical to a correlation receiver. In these cases, the choice of a suitable filter is strongly dependent upon the characteristics of the received signals [1]. By the same token, the standard back-projection method is a correlation of the data with the impulse response of the data acquisition process [13]. The approach presented here is quite different from the above methods as, in our scheme, the bi-dimensional maps describe the spatial variations of the statistical properties of the signals acquired in the space and time domain. These changes are directly due to different physical effects that alter the statistical parameters. This different point of view allows to detect buried objects, reduce unwanted effects and getting additional information about the different nature of the buried

materials. In addition, the target can be either in the antenna near or far field region, and still the correlation maps provide meaningful results. The correlation maps have always been a technique widely used in different area of physics in order to achieve spectroscopic measurements. For example, in the astronomy it was efficient in the characterization of the interstellar medium (ISM) spectra acquired from astronomical observations [14, 15]. In these measurements, as well as in GPR, the object under investigation is mapped by a series of spectra. The maps generated are characterized by a three dimensional coordinate system, with two axes describing the position while the third represents the frequency of the signal acquired. The reflections, the scattering effects and the material dispersion induce changes in the electromagnetic signals. These changes are directly observable on the level of mutual coherence/correlation between the acquired electromagnetic waves. This approach is quite general to be used in all cases where spectral line or data-cube signals are measured, even in time domain. In our work we extended and improved the method presented in [14, 15]. In the following sections it will be described how the interference of the reflected and scattered electromagnetic fields can influence the coherence level and how the maps can be deduced. Experimental results and a brief description of the measurement set-up are finally reported.

2. THE THEORY

In a wide-band GPR acquisition the finite size of the radiation pattern of the antenna and the presence of multiple reflections and scattering waves diffracted from the objects, induce clutters and de-focusing effects that alter the object image making difficult its recognition. During a mono-static acquisition the same antenna is used to feed and receive the reflected electromagnetic signal in each point of scanned surface. In a continuous wave approach the reflection coefficient (the ration between the reflected and incident waves) is measured. In our work this is directly done by means of a VNA. The reflection coefficient, measured by the VNA at the point $\mathbf{r}_i$, can be seen as the convolution of the antenna radiation diagram $D(\mathbf{r})$ with the received electromagnetic field $E^{rec}(\mathbf{r}, t)$ along the main polarization; the latter is the superimposition of the reflected and scattered fields from the target and surrounding objects:

$$\rho_i\left(t, \Delta\mathbf{r}\right) = \; D\left(\mathbf{r}\right) * E_i^{rec}\left(\mathbf{r}', t\right). \tag{1}$$

In writing the Eq. (1) we have considered a single polarization of the e.m. field. Assuming that the medium is no time-varying and a

radiation pattern characterized by an even distribution (with respect to the axis of the antenna in the $\mathbf{r}(y,z)$ plane), the convolution operator is equivalent to the correlation function [20]:

$$\rho_i\left(t,\Delta\mathbf{r}\right)=\left\langle D\left(\mathbf{r}\right),E_i^{rec}\left(\mathbf{r}',t\right)\right\rangle_r. \tag{2}$$

For the sake of simplicity, we consider only the (y,z) plane but the analysis can be extended in the whole space. The level of coherence of two signals acquired in two different positions $\mathbf{r}_i$, $\mathbf{r}_j$ is described by the time correlation function:

$$\left\langle \rho_i\left(t\right),\rho_j\left(t'\right)\right\rangle_t=\left\langle \left\langle D\left(\mathbf{r}\right),E_i^{rec}\left(\mathbf{r}',t\right)\right\rangle_r,\left\langle D\left(\mathbf{r}\right),E_j^{rec}\left(\mathbf{r}',t'\right)\right\rangle_r\right\rangle_t. \tag{3}$$

The subscripts $\mathbf{r}$ and t in the Eq. (3) denote the spatial and time correlation domain, respectively, whereas the dependence of the reflection coefficient on the spatial variables $\Delta\mathbf{r}=\mathbf{r}-\mathbf{r}$ has been omitted for simplicity. Thanks to the correlation properties [20], the Eq. (3) can be rewritten as:

$$\left\langle \rho_i\left(t\right),\rho_j\left(t'\right)\right\rangle=\left\langle\left\langle D\left(\mathbf{r}\right),D\left(\mathbf{r}'\right)\right\rangle,\left\langle E_i^{rec}\left(\mathbf{r},t\right),E_j^{rec}\left(\mathbf{r}',t'\right)\right\rangle\right\rangle. \tag{4}$$

The behavior of the cross-correlation function $<\rho_i,\rho_j>$ is strongly dependent on the antenna pattern radiation and in particular on the level of cross-coherence of the electromagnetic field received in different points (if the points are the same we will deal with the auto-correlation property of the signal). The stationary and variable contributions can be separated in two terms. The relation $<D(\mathbf{r}),D(\mathbf{r})>$ is the autocorrelation of the radiation pattern, not affected by the antenna position and by the external conditions, whereas the function $<E_i^{rec},E_j^{rec}>$ defines the changes in the correlation function by varying the observation point and the boundary conditions.

From the Eq. (4), we can deduce the statistical parameters that are dependent on: i) the presence of inhomogeneities in the soil, ii) the interference of the reflected and scattered waves and iii) the attenuation of the electromagnetic signals. These effects change the level of mutual correlation and coherence between the plane wave packets.

The correlation function of the received field along the z direction can be evaluated for the sake of simplicity according to the schematic depicted in Fig. 1(b), in which the received signal consists of many elementary waves emanating from different depths z and a wave directly reflected from the buried object. A single incident plane wave with a wavenumber k is considered, whereas the scattering profile is denoted with $a(z)$ and the reflected signal from the buried object has an amplitude a_R. The amplitude of the received signal in the point $\mathbf{r}_i$

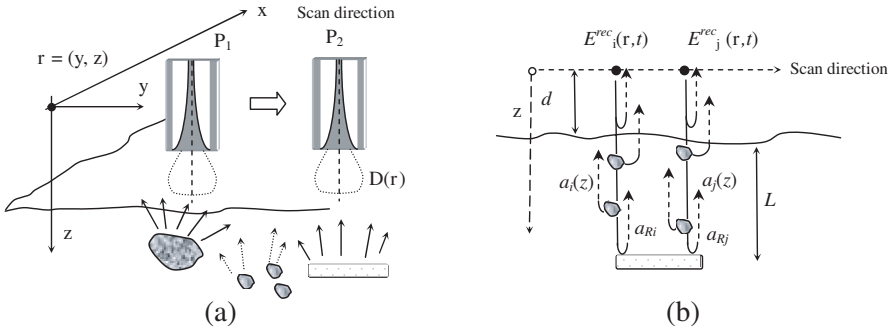

Figure 1. (a) Acquisition scheme and (b) interference effects of the reflected and scattering signals; for each point in the plane (x, y) there is a scattering profile $a_{i,j}(z)$ that describes the amplitude of the reflection coefficient.

along the z-direction is equal to [17]:

$$E_i^{rec}(k) = a_R e^{j2k(n\, z_L + d)} + \int_0^{\infty} a(z)\, e^{j2k\,(n\, z + d)} dz. \tag{5}$$

In the Eq. (5), we have assumed that the origin of the axis coincides with the receiving antenna, a spectral amplitude distribution equal for each incident wavenumber and a soil having a mean refractive index n. Otherwise noted, the terms a_R, $a(z)$, $n(z)$ and z_L depend on the position $\mathbf{r}_i$. The expression can be generalized by integrating the received field in the volume and assuming a refractive index $n(z)$ dependent on the depth. With these assumptions the auto-correlation function of the received field can be expressed in k-domain as:

$$\begin{aligned} &\langle E_i^{rec}(k), E_i^{rec}(k)^* \rangle \\ &= \left\langle |a_R(k)|^2 \right\rangle \qquad (i) \\ &\quad + 2\int_0^{\infty} \langle a_R a \rangle \cos\left(2kn\,(z - z_L)\right) dz \qquad (ii) \\ &\quad + \int_0^{\infty}\int_0^{\infty} \left\langle a(z)\, a\left(z'\right)^* \right\rangle e^{j2kn\,(z - z')} dz dz' \qquad (iii) \end{aligned} \tag{6}$$

The function $< |E_i^{rec}(k)|^2 >$ is the power spectral density of the received signal from which we can deduce the correlation function by

means of the inverse transform operator. The right-side member of the Eq. (6) is the contribution of three terms:

(i) the spectral density related to the reflectivity of the object (the dependence on wavenumber k is introduced in order to consider the dependence on the frequency);

(ii) the interference between the reflected signal (the position z of the scattered event is encoded in the frequency $2nz$ of the cosine function) and the scattering waves. The scattering points closeness the reference object alter in a more relevant way the level of coherence of the signal received.

(iii) the mutual interference between all the scattering waves;

Being the functions a_r and $a(z)$ equal to zero for $z < 0$, we replace them by a symmetric expansion ($a^{\wedge}(z)$, $a_R^{\wedge}$) respect to the origin and rewrite the Eq. (6) as [17]:

$$\begin{aligned} &\langle E_i^{rec}(k), E_i^{rec}(k)^* \rangle \\ &= \left\langle \left|\widehat{a}_R(k)\right|^2 \right\rangle + \frac{1}{2} Fourier\left\{\langle \widehat{a}_R \widehat{a}^* \rangle\right\} + \frac{1}{8} Fourier\left\{AC(\widehat{a})\right\} \end{aligned} \quad (7)$$

where AC ($a^{\wedge}(z)$) is the auto-correlation of the scattering profile. In the above equation the following relations have been introduced:

$$\begin{aligned} Fourier\left\{\langle \hat{a}_R \hat{a}^* \rangle\right\} &= \int_{-\infty}^{\infty} \langle \hat{a}_R \hat{a}^* \rangle \, e^{-j2kn(x-z_L)} dx \\ Fourier\left\{AC(\hat{a})\right\} &= \int_{-\infty}^{\infty} \langle \hat{a}\hat{a}^* \rangle \, e^{-j2knx} dx \\ \int_0^{\infty}\int_0^{\infty} \left\langle a(z)\, a\left(z'\right)^* \right\rangle e^{j2kn(z-z')} dz dz' &= \frac{1}{4} \int_{-\infty}^{\infty} AC\left(\hat{a}(x)\right) e^{j2knx} dx \,. \end{aligned} \quad (8)$$

The Eq. (8) can be extended to the signals acquired in two adjacent points $\mathbf{r}_i$ and $\mathbf{r}_j$. by means of the following relation:

$$\begin{aligned} \left\langle E_i^{rec}(k), E_j^{rec}(k)^* \right\rangle &= \left\langle \left|\hat{a}_R(k)\right|^2 \right\rangle + \frac{1}{2} Fourier\left\{\langle \hat{a}_R \hat{a}_i^* \rangle\right\}^* \\ &+ \frac{1}{2} Fourier\left\{\left\langle \hat{a}_R \hat{a}_j^* \right\rangle\right\} + \frac{1}{8} Fourier\left\{CC\left(\hat{a}_i, \hat{a}_j^*\right)\right\}. \end{aligned} \quad (9)$$

The function CC ($a_i^{\wedge}(z)$, $a_j^{\wedge}(z)*$) is the cross-correlation function of the scattering profiles a_i and a_j. In deriving Eq. (9) it was assumed that $z_L^i = z_L^j$ and $a_R^i = a_R^j$ (see Fig. 1(b)). The presence of scattering

waves changes the correlation function and hence the level of coherence of the electromagnetic field received (see Eqs. (8), (10)). The additional terms, due to interference effects, can be more or less relevant according to the behavior of the correlation functions. For example, in presence of strongly scattering surface, the autocorrelation term in Eq. (7) — or equivalently the mutual interference between the scattered wave in Eq. (9) — is weaker than the $< a_R^{\wedge}, a^{\wedge *} >$, as the scattering will be highly un-correlated and the outer lobes of the correlation function very weak.

3. THE CORRELATION MAPS

The signals acquired in the time domain generate a data cube characterized by a three dimensional coordinate system, with two axes describing the position and the third representing the time coordinate or equivalently the depth (see Fig. 2). From the data collected it is possible to extract, depending on the "observation point", the time and spatial variation of the received fields along the three coordinates (Fig. 2(b)).

As highlighted by Eqs. (7), (8), the time coherence of the received signal is affected by the mutual interferences of the electromagnetic signals. Each variation in the amplitude and energy of the signals can be revealed by their variance σ_i:

$$\sigma_i = \langle E^{rec}(t, \mathbf{r_i}), E^{rec}(t + \Delta t, \mathbf{r_i}) \rangle|_{\Delta t=0}. \tag{10}$$

Differently, a variation in the shape of the density power of spectrum is related to a change in the degree of coherence due to

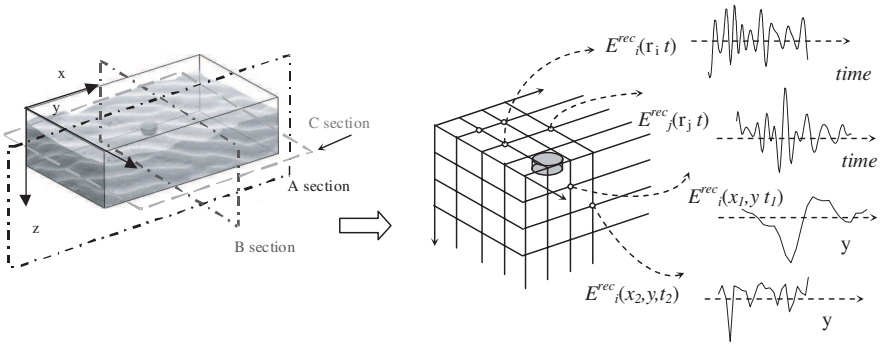

(a) (b)

Figure 2. (a) Acquisition scheme and definition of the A, B C sections, (b) the discrete acquisition generates a data cube.

the mutual interferences; the broader the spectrum width $\Delta\nu$ of the source, the narrower its degree of coherence. The coherence time τ_c is a quantitative measure of the coherence degree. A convenient definition of the time coherence of a signal having a power spectrum density $S(\nu)$, is the relation [18]:

$$\tau_c = \frac{\int_0^\infty S^2(\nu)}{\left(\int_0^\infty S(\nu)\right)^2}. \tag{11}$$

The relationship existing between two random signals acquired in different positions can be described by their covariance σ_{ij} or more in detail, by the cross-correlation coefficient (Pearson coefficient) c_{ij}:

$$\sigma_{ij} = \langle E^{rec}(t, \mathbf{r_i}), E^{rec}(t+\Delta t, \mathbf{r_j})\rangle|_{\Delta t=0} \quad c_{ij} = \frac{CC\left(E_i^{rec}, E_j^{rec}\right)}{\sigma_i^{rec}\sigma_j^{rec}} \tag{12}$$

where E_i^{rec} and E_j^{rec} define the signal acquired in $\mathbf{r}_i$ and $\mathbf{r}_j$ respectively, whereas σ_i and σ_j are their variances. In Fig. 3, it is reported the

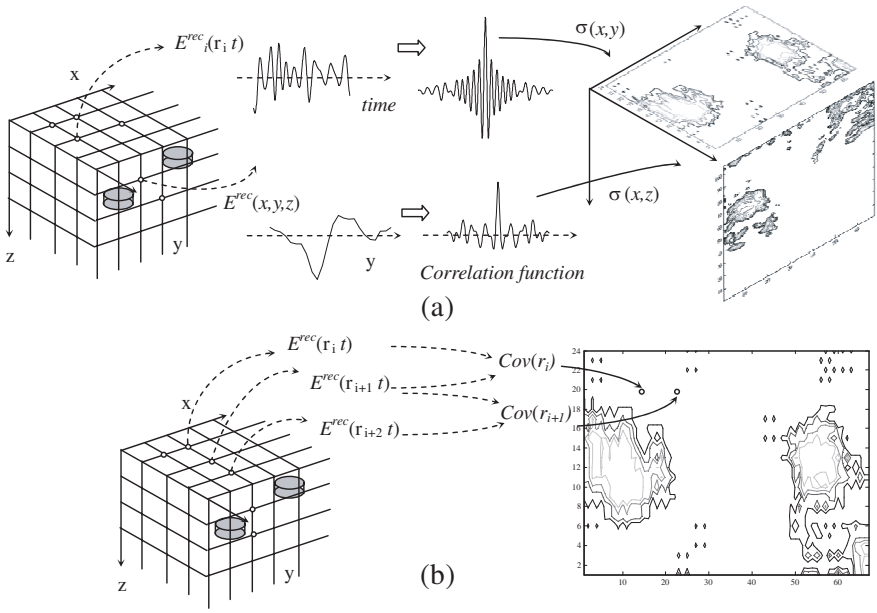

Figure 3. Example of definition of a map describing the (a) auto-correlation (variance map) and the (b) cross-correlation (covariance) properties.

scheme applied in order to create the maps that describe the spatial variations of the statistical parameters introduced. For each point of the plane (x, y), (x, z) or (y, z), the time/spatial signal variation is extracted and the variance together with the time coherence are evaluated from the auto-correlation function.

In the analysis of the coherence level between different signals, the correlation is done sequentially between adjacent points. For example, the value of the statistical parameter in the point $\mathbf{r}_i$ of the map, is obtained from the cross-correlation function of the signals in $\mathbf{r}_i$ and $\mathbf{r}_{i+1}$, considering the plane x-y in the data-cube (Fig. 3(b)).

In this method, the information collected in a data cube is transformed and synthesized in a bi-dimensional image that has the property to condensate the relevant features in only one section, in particular in the x-y, y-z and x-z planes. These maps are generated by changing the direction along which the data-cube is observed. This approach is quite different from [14, 15] and it can be applied if the signals acquired feature a proper level of spatial correlation.

4. EXPERIMENTAL RESULTS

The experimental results have been obtained by means of the GPR system reported in Fig. 4, made by a VNA (Agilent E5071C, ENA series), working basically as an ultra-wideband radar with synthetic pulse: the measured frequency behavior of the reflection coefficient across a wide-band antenna is processed by inverse FFT and filtered providing a measurement of the reflected pulse in time domain. The

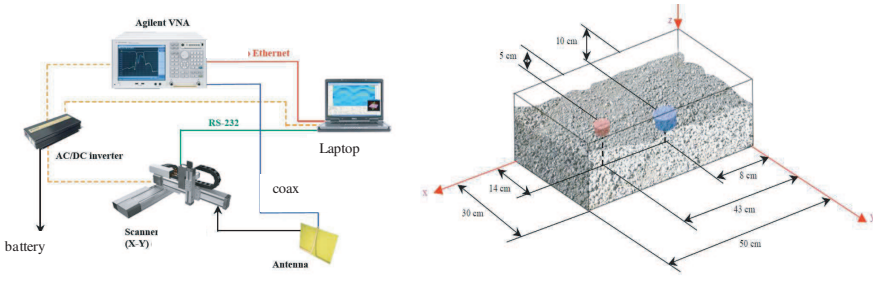

Figure 4. (a) Experimental set-up and (b) test performed using two metal targets of different size and at different depth: the first one is a cylinder having 5 cm diameter and at 5 cm from the surface and the second one featuring 10 cm diameter at 10 cm from the surface. The targets were buried in gravel (grain size > 2 mm).

VNA is an instrument able to measure the scattering parameters, namely magnitude and phase of the reflection and transmission coefficients on a microwave or millimeter wave circuit. VNA have been used several times in the GPR context in the past [19]. In our device the ENA E5071C features a bandwidth of 8.5 GHz, and includes an embedded time-domain module to perform FFT and hence to speed-up acquisition.

The antenna is a broadband printed structure, similar to a Vivaldi antenna but designed by exploiting both sides of the substrate (FR4), as shown in Fig. 4, optimized by finite element simulations (Ansoft HFSS) as well as method-of-moments modeling (MEM Research EM3DS). The antenna was synthesized in such a way to match the impedance of the coaxial feeding line (50 Ohms) to the wave impedance of the soil over the widest possible band. In our case, the dielectric permittivity of dry sand was considered and the antenna was optimized to reduce its performance deterioration induced by modifications of the operating conditions [19], e.g., radiation over different terrains (see Fig. 5) and at different distances. At the end of a measurement process a 3D matrix is obtained: the scanner moves the antenna in x and y while z data are obtained considering the temporal evolution of echo, in turn derived by inverse FFT of the reflection coefficient. Sections of such a matrix are labeled as A, B and C section, according to what defined in Fig. 2 (note: usually "A-B-C scans" are respectively used to indicate mono, bi- and tri-dimensional scans). The measured reflection coefficient is processed by inverse Fourier transform, and windowing by either Hamming or Kaiser-Beta: most of these actions are directly implemented in the VNA.

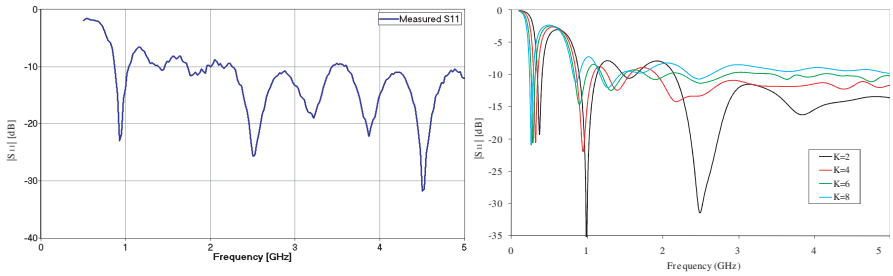

(a) (b)

Figure 5. (a) Measured reflection coefficient in sand and antenna designed for GPR operation in the inset, (b) simulated reflection coefficient for different soils. The range of permittivity considered, characterizes the majority of dry soils.

Tests were performed using two metal targets of different size and at different depth: the first one is a cylinder having 5 cm diameter at 5 cm from the surface; the second one featuring 10 cm diameter is at 10 cm from the surface. The targets were buried in gravel (grain size > 2 mm) as reported in Fig. 4(b). This makes clutter even more relevant. The small stones composing the gravel, produce their own visible echo, so gravel is a challenging environment where clutter is high. In sand, excellent images were generally obtained even by raw data, as expected. Moreover our antenna was optimized considering radiation over sand, and this test in gravel also highlights the capability to obtain results in different operating conditions. In Figs. 6(a) and 6(b), it is reported the x-y plane raw data at 10 cm and 5 cm depths, respectively. Scans are purposely performed at reduced spatial resolution, as needed to reduce the scanning time.

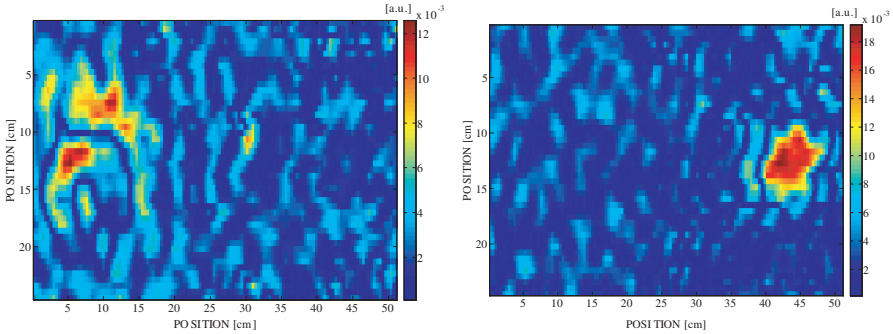

Figure 6. Raw data: reflection coefficient at (a) 10 cm and (b) 5 cm depth.

The information collected in a data cube are transformed, according to the scheme reported in Fig. 2, into a bi-dimensional image that has the property to visualize the relevant features in one section. The presence of buried object is highlighted by an increase of the correlation level and the coherence time of the signals acquired in the plane x-y (see the maps in Fig. 7(a) and Fig. 7(c)), whereas the distribution of the time shift of the peak of the correlation function, reported in the map in Fig. 7(b), is quite uniform. Although the targets are placed at different depths in environment where the presence of clutters is relevant, the received signals show similar level of coherence nearby the targets.

It is rather important to note that, working in the near-field region and being in presence of an high level of echoes, the information relative to the shift of the peak of the correlation function, that is proportional

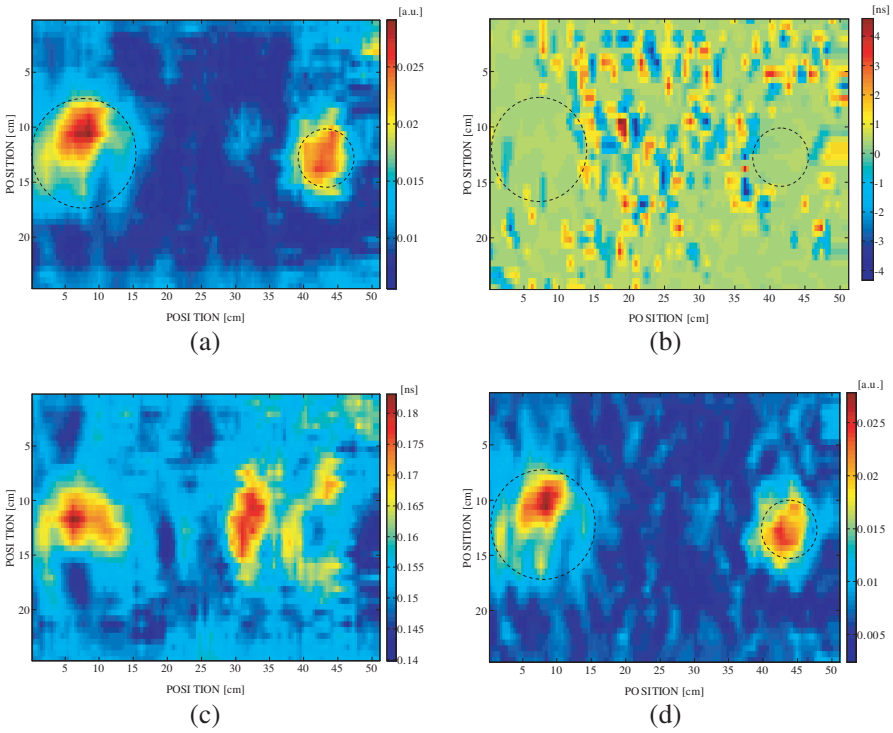

Figure 7. Maps of: (a) variance, (b) time shift (ns) of the correlation function peak, (c) the coherence time (ns), (d) the covariance. The dotted line contours the buried objects.

to the signal time delay, does not give a clear information about the position and the shape of the objects. Differently, the spatial variation of the variance and the time coherence highlight the presence of the buried targets, without describing accurately the shape and the correct dimensions of objects. The same effects appear when considering the level of correlation of the signals acquired in adjacent points on the plane x-y, as reported in the covariance map in Fig. 7(d). In fact, the covariance of two random variables characterizes not only their dependence but also their dispersion (variance). The normalization introduced in the Eq. (12) makes the term c_{ij} dependent only on the level of correlation existing between the variables. This allows to describe the linear relationship existing between the signals, enhancing the contour of the targets and improving the contrast (Fig. 9(a)). The map obtained shows that the signals acquired over the buried object are characterized by a more pronounced value of linear correlation.

According to the aforementioned results, the signals directly reflected from the objects have an higher value of variance and an increased time coherence delay. This information can be combined in a single map by plotting the variation of the shape of the central lobe of the correlation function, described by a time shift, at a specific reference value (see Fig. 8).

Figure 9(b) shows the data obtained following the scheme in Fig. 8. The echoes are reduced and the contour of the targets appear more distinct respect to the image in Fig. 9(a). The main advantage of the correlation maps resides in the possibility to compensate the different depths of the targets. In fact, as can be seen in Fig. 6(a), the raw data of the deeper object appear more perturbed by the attenuation, scatterings and echoes than the shallow target in Fig. 6(b). The coherence level of the signals structured in a data cube can be analyzed along different directions (see Fig. 3), simply by changing the

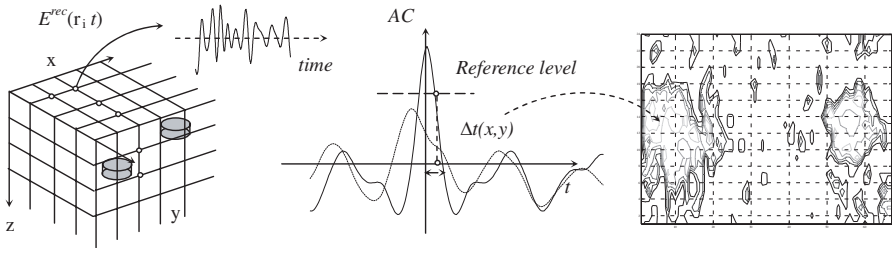

Figure 8. Scheme for the acquisition of the time delays for a fixed value of correlation. AC: auto-correlation function and Δt: time shift.

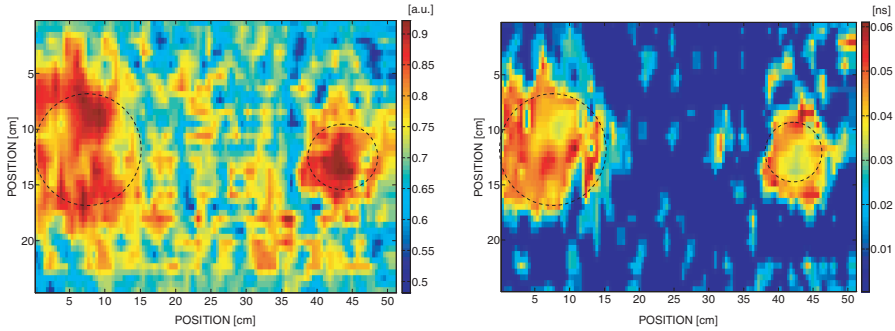

Figure 9. (a) Map of the cross-correlation coefficient. (b) Map obtained according to the scheme in Fig. 8. The reference level is 80% of the maximum of data reported in Fig. 6(a).

observation point and evaluating for each time instant (or depth value) the correlation functions along the y or x directions. In this way, the maps in the plane x-z and y-z are generated and the acquisition is made "virtually" along a different direction in the space thanks to a proper level of spatial correlation featured by the e.m. fields acquired in the points of the plane x-y.

In order to evaluate quantitatively the performance of the approach, the signal-to-background ratio SBR, defined as in [16], was used:

$$SBR = \left(\frac{\sum_{i \in D, j \in Rs} \max\left(|s_{i,j}(t)|^2 \right)}{\sum_{i \in D, k \in Rb} \max\left(|b_{i,k}(t)|^2 \right)} \right) \tag{13}$$

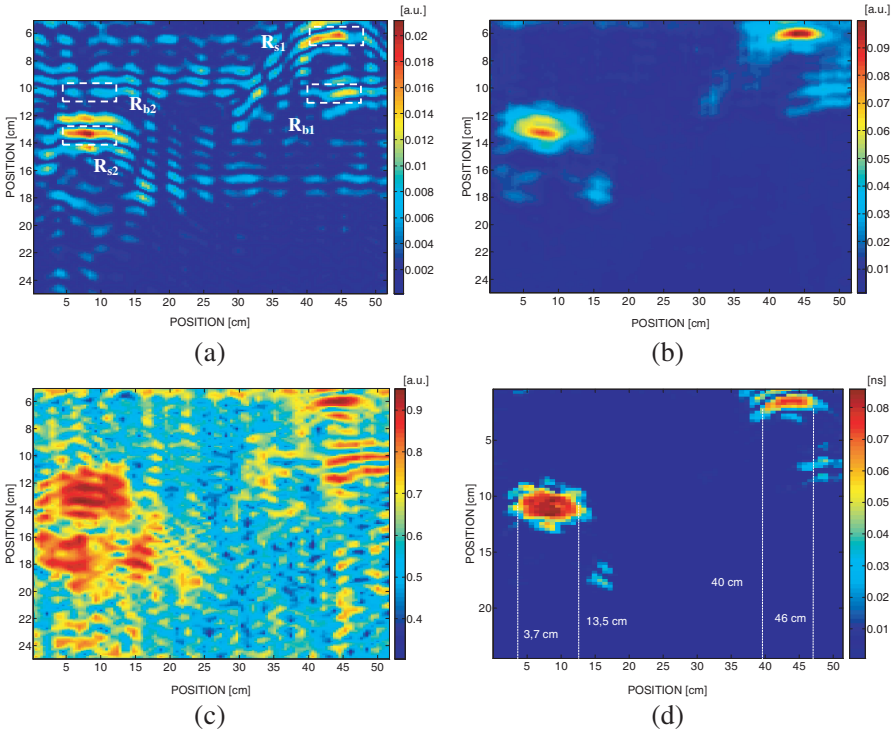

Figure 10. Maps relative to the (a) raw data, (b) variance, (c) cross-correlation coefficient and (d) time delay map: the reference level is 80% of the maximum of data reported in (b). The scale along the z-direction has been defined assuming a wave speed in the ground equal to $1.1 \cdot 10^8$ m/s.

Table 1. Signal-to-background ratio: SBR.

Data	SBR (R_{s1}, R_{b1})	SBR (R_{s1}, R_{b2})	SBR (R_{s2}, R_{b1})	SBR (R_{s2}, R_{b2})
Raw data	3.4 dB	5.6 dB	2.4 dB	3.7 dB
Averaging data	6.6 dB	8.2 dB	6.7 dB	10.3 dB
Cross-covariance function	7.2 dB	14 dB	8.6 dB	15.3 dB

where $s(t)$ is the desired target signal and $b(t)$ the background signal. Being the position of each target known, the signal region R_s was chosen coincident with it and centered at the apex of the target response (width = 5 cm). The same sizes were chosen for the background regions R_b, located in different position where the clutter signal appears more intense. The regions are displayed in Fig. 10(a) The results are reported in Table 1.

They show an improvement in the clutter reduction by applying the averaging and the correlation algorithm sequentially to the raw data. A further byproduct of the SCF algorithm is a focusing effect, shown in Fig. 10(b) and Fig. 10(d), and a reduction of the hyperbolic distortion appearing in the raw images.

5. CONCLUSION

This paper discusses the use of the correlation maps in the ultra-wideband GPR systems. This technique exploits the different level of coherence that characterizes the electromagnetic signals reflected and scattered from the objects when compared with clutter. By combining the information collected in the maps, relative to the variance and the coherence time of the received fields, it is possible to compensate the different depths of the targets, reducing the distortion and improving the image contrast. The analysis of the correlation behavior of the signals can be extended to each direction in the volume under investigation.

REFERENCES

1. Daniels, D. J., *Ground Penetrating Radar*, 2nd edition, IET, London, 2007.
2. Druyts, P., A. Merz, M. Peichl, and G. Triltzsch, "HOPE: Raising the reliability of mine detection through an innovative a handheld multi-sensor (MD, GPR, MWR) mine detector

prototype with imaging capabilities," *Proceedings of PIERS*, Singapore, Jan. 2003.

3. Crocco, L., F. Soldovieri, T. Millington, and N. J. Cassidy, "Bistatic tomographic GPR imaging for incipient pipeline leakage evaluation," *Progress In Electromagnetics Research*, Vol. 101, 307–321, 2010.
4. Roslee, M. B., R. S. A. Raja Abdullah, and H. Z. M. Shafr, "Road pavement density analysis using a new non-destructive ground penetrating radar system," *Progress In Electromagnetics Research B*, Vol. 21, 399–417, 2010.
5. Capineri, L., D. J. Daniels, P. Falorni, O. L. Lopera, and C. G. Windsor, "Estimation of relative permittivity of shallow soils by using the ground penetrating radar response from different buried targets," *Progress In Electromagnetics Research Letters*, Vol. 2, 63–71, 2008.
6. Ash, E. A. and G. Nicholls, "Super-resolution aperture scanning microscope," *Nature*, Vol. 237, 510–512, Jun. 1972.
7. Farina, M., et al., "Algorithm for reduction of noise in ultra-microscopy and application to near-field microwave microscopy," *IET Elect. Lett.*, Vol. 46, No. 1, 50–52, Jan. 2010.
8. Van der Merwe, A. and I. J. Gupta, "A novel signal processing technique for clutter reduction in GPR measurement of small, shallow, land mines," *IEEE Trans. on Geosci. Remote Sens.*, Vol. 38, No. 6, 2627–2637, 2000.
9. Yakubov, V. P. and D. Y. Sukhanov, "Solution of a subsurface radio-imaging inverse problem in the approximation of a strongly refractive medium," *Radiophysics and Quantum Electronics*, Vol. 50, No. 4, 299–307, 2007.
10. Stolt, R. H., "Migration by Fourier transform," *Geophysics*, Vol. 43, No. 1, 23–48, Feb. 1978.
11. Atteia, G. E. and K. F. A. Hussein, "Realistic model of dispersive soils using PLRC-FDTD with applications to GPR systems," *Progress In Electromagnetics Research B*, Vol. 26, 335–359, 2010.
12. Chen, H., R. Wu, J. Liu, and Z. Han, "GPR migration imaging algorithm based on NUFFT," *PIERS Online*, Vol. 6, No. 1, 16–20, 2010.
13. Fool, S. and S. Kashyap, "Cross-correlated back projection for UWB radar imaging," *Antennas and Propagation Society International Symposium IEEE*, Vol. 2, 1275–1278, 2004.
14. Rosolowsky, E. W., A. A. Goodman, D. J. Wilner, and J. P. Williams, "The spectral correlation function: A new tool

for analyzing spectral line maps," *The Astrophysical Journal*, Vol. 524, 887–894, 1999.

15. Schneider, J., P. Amaro-Seoane, and R. Spurzem, "Higher order moment models of dense stellar systems: Applications to the modeling of the stellar velocity distribution function," *Mon. Not. R. Astron. Soc.*, Vol. 2, 1–2, 2010.
16. Mayordomoet, A. M., et al., "Optimal background subtraction in GPR for humanitarian demining," *EuRAD 2008*, 48–51, 2008.
17. Bouma, B. and G. Tearney, *Handbook of Optical Coherence Tomography*, Marcel Dekker, 2002.
18. Saleh, B. E. A. and M. C. Teich, *Fundamental of Photonics*, John Wiley & Sons, 1991.
19. Yarovoy, A., et al., "The dielectric wedge antenna," *IEEE Trans. Antennas Propagat.*, Vol. 50, 1460–1472, 2002.
20. Ventsel, E. S., *Theory of Probability*, Mir, Russia, Moscow, 1983.